OPEN ACCESS

Materials Chemistry ARTICLE

The Innovation Materials

Interaction-density-directed supramolecular engineering in lignin toward adhesive–porous composite materials

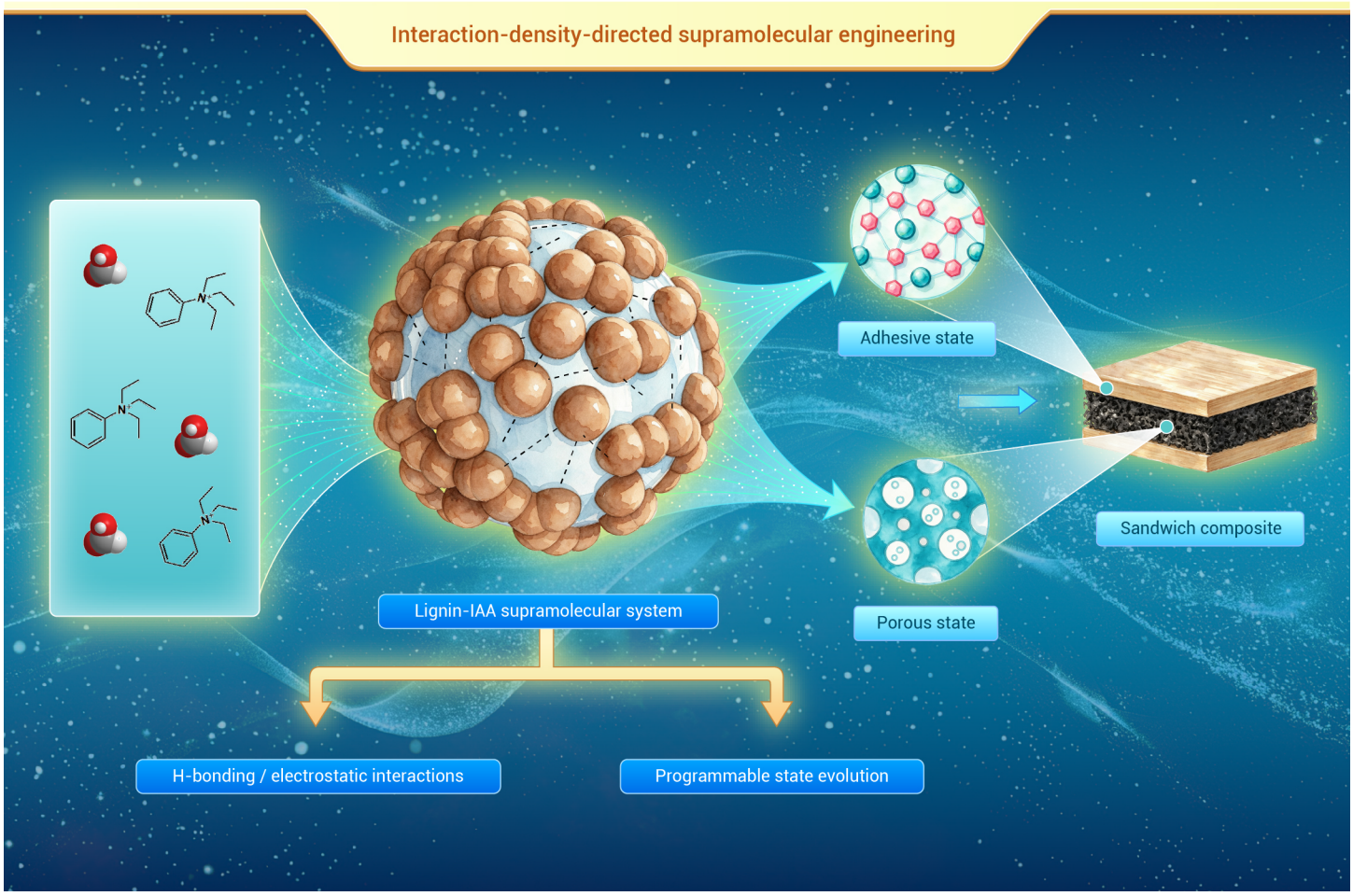
Xin-Yi Hui,[1,2] Cheng Zuo,[1,2] Ji-Yun Qi,[1,2] Chu-Wan Liang,[2] Tong Zhou,[1,2] Xiaojun Shen,[3] Jia-Long Wen,[1,2,*] and Tong-Qi Yuan[1,2]

*Correspondence: wenjialong@bjfu.edu.cn

Received: May 6, 2026; Accepted: September 8, 2026; Published Online: September 8, 2026; https://doi.org/10.59717/j.xinn-mater.2026.100243

© 2026 The Author(s). This is an open access article under the CC BY license (https://creativecommons.org/licenses/by/4.0/).

GRAPHICAL ABSTRACT



PUBLIC SUMMARY

- Interaction-density regulation directs lignin into adhesive- or porous-dominated material states.
- The KL-based adhesive reaches a lap shear strength of 5.46 ± 0.12 MPa at room temperature.
- Lignin-derived adhesive and porous components enable multifunctional sandwich composites.

ARTICLE Materials Chemistry

OPEN ACCESS

www.the-innovation.org/the-innovation-materials

Interaction-density-directed supramolecular engineering in lignin toward adhesive–porous composite materials

Xin-Yi Hui,[1,2] Cheng Zuo,[1,2] Ji-Yun Qi,[1,2] Chu-Wan Liang,[2] Tong Zhou,[1,2] Xiaojun Shen,[3] Jia-Long Wen,[1,2,*] and Tong-Qi Yuan[1,2]

[1]State Key Laboratory of Efficient Production of Forest Resources, Beijing Forestry University, Beijing 100083, China

[2]Beijing Key Laboratory of Lignocellulosic Chemistry, Beijing Forestry University, Beijing 100083, China

[3]Leibniz-Institut fur Katalyse eV, Rostock 18059, Germany

*Correspondence: wenjialong@bjfu.edu.cn

Received: May 6, 2026; Accepted: September 8, 2026; Published Online: September 8, 2026; https://doi.org/10.59717/j.xinn-mater.2026.100243

© 2026 The Author(s). This is an open access article under the CC BY license (https://creativecommons.org/licenses/by/4.0/).

Citation: Hui X., Zuo C., Qi J., et al. (2026). Interaction-density-directed supramolecular engineering in lignin toward adhesive–porous composite materials. *The Innovation Materials* **4**:100243.

Achieving structurally integrated adhesive and porous materials from heterogeneous biopolymers remains challenging because current strategies typically rely on covalent modification, multicomponent blending, or separately processed constituents. Here, we report an interaction-density-directed supramolecular engineering strategy to derive adhesive and porous architectures from a single lignin platform. Driven by enhanced hydrogen-bonding and electrostatic interactions, an interfacial amphiphilic agent (IAA)-mediated lignin network exhibits restricted chain mobility, enabling rapid interfacial locking at room temperature. In this regime, the lignin system functions as a strong supramolecular adhesive with lap shear strengths of up to 5.46 MPa. By combining pre-oxidation with reduced effective interaction density and thermal activation, the same platform is redirected into a porous architecture featuring low density, high specific surface area, low thermal conductivity, and enhanced flame retardancy. Because both the adhesive and porous components are derived from the same lignin-based supramolecular platform, they can be assembled with wood veneers into a sandwich composite comprising veneer facings, adhesive interlayers, and a multifunctional porous foam core for bonding, thermal insulation, flame retardancy, and formaldehyde capture.

INTRODUCTION

The ability to precisely control material state and architecture across multiple length scales is a central objective in modern materials science.[1] Many advanced applications, ranging from load-bearing panels and thermal insulation to fire-resistant and air-purifying structures, require the spatial integration of dense solid regions and porous architectures within a single material system.[2] However, such integration is typically achieved through multicomponent composites or sequential assembly of chemically distinct materials, often resulting in interfacial incompatibility, complex processing, and limited recyclability.[3] Developing a single material platform capable of programmable state control and structural integration therefore represents a fundamental challenge.

Most existing strategies for integrating solid and porous structures rely on covalent crosslinking, processing in multiple steps, or blending with polymers derived from petroleum.[4,5] While effective in some cases, these approaches often lead to complex fabrication processes and limited flexibility in structural design. More critically, they decouple structural programmability from material performance, treating solid and porous components as independent entities rather than as different manifestations of a unified material system. This paradigm fundamentally limits the design of multifunctional and adaptable materials.

Biopolymers provide a promising foundation for sustainable materials due to their abundance, renewability, and intrinsic functionality.[6,7] Among them, lignin stands out as the most abundant renewable aromatic polymer, featuring a rigid backbone, high carbon content, and inherent flame-retardant characteristics, and has been increasingly explored as a feedstock for bio-based polymers and lignin valorization.[8-12] Despite these advantages, lignin has long been regarded as one of the most challenging biopolymers to process. Its structural heterogeneity, strong intermolecular aggregation, and poor solubility severely restrict controlled assembly, making it difficult to access diverse material architectures without extensive chemical modification or blending.[13] To address lignin recalcitrance, previous efforts have primarily focused on covalent chemical modification or copolymerization strategies, which can improve the processability of lignin-based materials but often compromise their sustainability and scalability.[14,15] Recent advances in adhesive materials have highlighted the importance of regulating interfacial interactions, network dynamics, and molecular mobility for achieving strong, durable, and processable bonding performance.[16,17] An alternative paradigm is supramolecular regulation, where material properties and architecture are governed by noncovalent interactions rather than permanent chemical bonds.[18,19] From this perspective, lignin should be viewed not as a fixed precursor for a specific product, but as a dynamic supramolecular system whose assembly state can be programmed through interaction control.

Herein, we present an interaction-density-directed supramolecular engineering strategy that enables a single lignin-based system to access multiple functional material states. By introducing an interfacial amphiphilic agent (IAA) composed of formic acid (FA) and benzyltriethylammonium chloride (TEBAC), we regulate cooperative noncovalent interactions in lignin without covalent backbone modification (Figure 1A). In this work, interaction density is used as an apparent descriptor of the effective supramolecular interaction state in the lignin–IAA network, as reflected by interaction-domain continuity, interaction strength, and the restriction of lignin mobility. Subsequently, by adjusting the interaction density and processing conditions, the same formulation can be directed toward adhesive- or porous-dominated states (Figure 1B). The lignin-derived adhesive and porous components are subsequently assembled with wood veneers into a multifunctional sandwich structure (Figure 1C). Practical bonding demonstrations and comparisons of bonding performance and preparation time are presented in Figures 1D-F.

MATERIALS AND METHODS

Materials. Alkali lignin (AL) is derived from the black liquor of Longli Pulp and Paper Company. Softwood kraft lignin (KL) and hydrolyzed lignin (HL) are obtained from industrial pulp and paper waste liquor. 3-Chloro-2-hydroxypropyltrimethylammonium chloride (CHPTAC, 65%), benzyltriethylammonium chloride (TEBAC, 98%), choline chloride (ChCl, 98%), sodium dodecylbenzenesulfonate (SDBS, 90%), Tween-20 (99%), formic acid (FA, 99.5%), and formaldehyde (HCHO, 37%) were purchased from Shanghai Macklin Biochemical Co., Ltd. (Shanghai, China). Beech wood boards, glass plates, and ceramic dishes were all purchased from Taobao.

Preparation of Interfacial Amphiphilic Agent (IAA). With the mass of TEBAC held constant, the amount of FA was varied to obtain FA mass ratios of 1:2, 1:1, and 2:1. The mixtures were stirred at 80°C until clear and homogeneous. For comparison, different IAA solutions were prepared using CHPTAC, SDBS, ChCl, and Tween-20 with FA following the same procedure.

Preparation of Supramolecular Lignin Adhesives. The prepared IAA was mixed with alkali lignin AL at mass ratios of 1:1 and 2:1. The mixture was stirred for 10 min until a uniform black liquid was formed and stored at room temperature.

Preparation of Pre-oxidized Lignin. A measured amount of alkali lignin (AL) was placed in a muffle furnace with a heating rate of 10°C/min and treated at different temperatures (130, 140, and 150°C) for 2 h. After cooling naturally to room temperature, the samples were labeled as AL-130, AL-140, and AL-150, and stored in sealed containers at room temperature.

Preparation of Supramolecular Lignin Foam. 6 g of pre-oxidized lignin was accurately weighed and transferred into a beaker. The prepared IAA was then

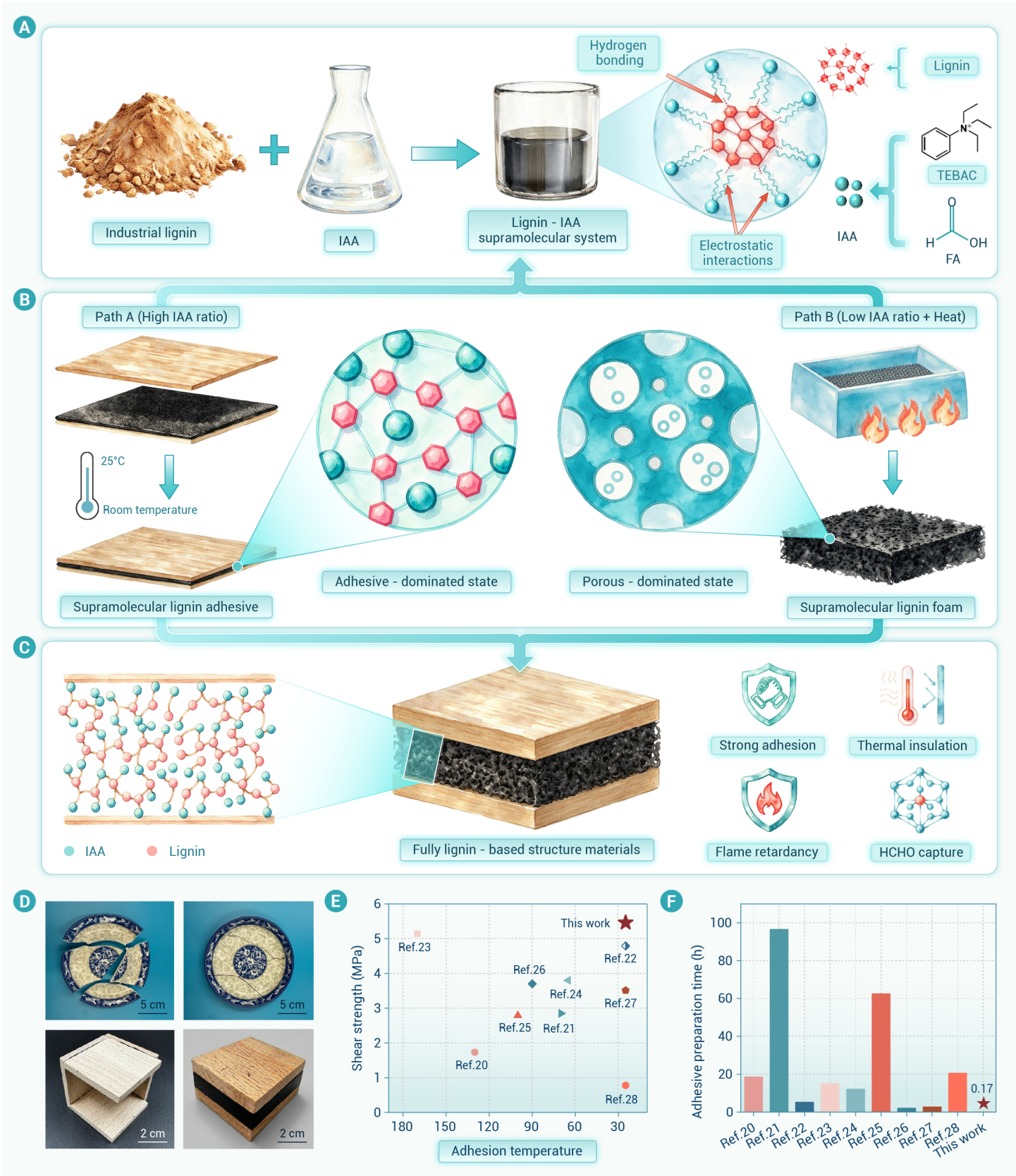


Figure 1. Interaction-density-directed supramolecular engineering of lignin for adhesive–porous integrated composite materials (A) Formation of a lignin–IAA supramolecular system by combining industrial lignin with an IAA composed of formic acid (FA) and benzyltriethylammonium chloride (TEBAC), enabling regulation of hydrogen bonding and electrostatic interactions. (B) Divergent processing pathways directed by interaction density. High IAA ratios (Path A) generate an adhesive-dominated solid state with strong room-temperature bonding, while reduced effective interaction density combined with thermal activation (Path B) redirects the system toward a porous architecture. (C) Integration of adhesive and porous components derived from the same lignin-based supramolecular platform with wood veneers to construct a sandwich composite comprising veneer facings, adhesive interlayers, and a porous foam core for mechanical adhesion, thermal insulation, flame retardancy, and HCHO capture. (D) Photographs demonstrating repair of a fractured ceramic plate, fabrication of a load-bearing wooden component, and assembly of the sandwich composite using the supramolecular lignin materials. (E) Comparison of lap shear strength and adhesion temperature with reported lignin-based adhesives, demonstrating strong room-temperature bonding.[20-28] (F) Comparison of adhesive preparation time, showing the rapid processability of the lignin adhesive system.

added at 15, 22.5, and 30 wt% relative to the mass of pre-oxidized lignin. The mixture was homogenized and subsequently poured into a circular mold (3 cm in diameter) for compression molding under a pressure of 1 MPa. Following demolding, the samples were subjected to thermal treatment in a muffle furnace at 240°C for 2 h, with a controlled heating rate of 5 °C/min. Upon removal, the samples were allowed to cool naturally to room temperature. For comparison, samples without IAA were prepared using 6 g of AL or AL-140 following the same procedure.

Mechanical Testing of Wood Adhesion. Beech wood boards were sectioned into strips measuring 80 × 20 × 10 mm. The adhesive was applied to a bonded overlap area of 20 × 10 mm at a rate of 15 g/m^2. The samples were clamped and cured at ambient temperature for 24 h. Following curing, lap shear tests were performed using a universal testing machine in compliance with BS EN 205:2016. Ten independent bonded specimens were tested for each formulation, and the mean and standard deviation were calculated.

HCHO Adsorption Measurements. An appropriate volume of HCHO solution was introduced into a two-necked buffer flask, which was connected to a nitrogen cylinder to steadily deliver HCHO gas into a 9 L custom-built sealed chamber equipped with a continuous HCHO gas monitor. The HCHO concentration within the chamber was maintained at 30–35 ppm by regulating the gas flow rate. Subsequently, 5 g of the sample was weighed and evenly distributed in a 12 cm Petri dish, which was then placed in the chamber for continuous monitoring over 1 h. The HCHO concentration at time t was recorded as C_t. The HCHO removal efficiency (%) was calculated according to Equation (1):

$$\text{HCHO removal efficiency (\%)} = \frac{C_0 - C_t}{C_0} \times 100\% \quad (1)$$

where C_0 and C_t are the HCHO concentrations (ppm) before and after adsorption, respectively. For comparison among samples, the HCHO removal values reported in Table S8 were expressed based on an initial HCHO concentration of 30 ppm.

Rheological Measurements. The viscosity and modulus of the samples were measured using a rheometer (Anton Paar GmbH, Austria) at 20°C, with steady-state flow experiments performed using a 25 mm parallel plate over a shear-rate range of 0.01–1000 s^{-1}.

Structural and Chemical Characterization. Thermogravimetric analysis (TGA) and derivative thermogravimetric analysis (DTG) were conducted using a thermogravimetric analyzer (NETZSCH TG 209 F1 Libra, Germany). X-ray diffraction (XRD) patterns were recorded using an X-ray diffractometer with a scanning range of 10–80° and a scanning speed of 10°/min. The surface chemical composition was analyzed by X-ray photoelectron spectroscopy (XPS, ESCALAB 250Xi, Thermo Scientific, USA).

X-ray Micro-Computed Tomography (Micro-CT) Analysis. The wood blocks with applied coating samples were visualized using an X-ray Micro-CT system (Bruker SKYSCAN 2214, Belgium) operated at 50 kV and 1 W. The transmission grating was rotated over 360° to acquire X-ray micrographs, and beam hardening correction and three-dimensional reconstruction were performed using Dragonfly software.

Density Functional Theory (DFT) Calculation. The binding energy analysis was performed using Density Functional Theory (DFT). The molecular structures of four model systems were optimized. Frequency analysis was conducted using ORCA 5.0.3 software at the B3LYP-D^3/def2-TZVP basis set level. The molclus program was utilized to generate 2000 configurations for each combination. These combinations included AL, AL/FA (AL-F), AL/TEBAC (AL-T), and AL/FA/TEBAC (AL-F-T). The configurations were generated under optimal conditions to screen for the most stable structures. For the lower-energy configurations, further optimization and frequency analysis were carried out. These calculations were performed using ORCA 5.0.3 at the B3LYP-D^3/def2-TZVP level.[29] Single-molecule conformations without imaginary frequencies were then calculated. The higher-accuracy ωB97X-2-D^3(BJ)/def2-TZVPP level was used for these calculations. The wavefunction analysis program Multiwfn 3.8 dev was employed for additional analysis.[30] This included molecular surface electrostatic potential (ESP), intermolecular interaction energies, and the Independent Gradient Model (IGM).[31] Visualization of interactions was achieved using VMD 1.9.3.

Molecular Dynamics (MD) Simulations. Molecular dynamics (MD) simulations were conducted using GROMACS 2023 software.[32] The simulation system included 123 AL molecules, 175 benzyltriethylammonium cations, 175 Cl^-, 435 FA molecules, and 1194 water molecules. The box size was chosen to accommodate the specified number of molecules. Adjustments were made under the NPT ensemble. Detailed molecular counts for each system are provided in Table S10. Intra- and intermolecular interactions were modeled using the GAFF force field parameters. The RESP charges for the monomers were calculated using ORCA 5.0.3 software at the B3LYP/def2-TZVP level.[29] Charge assignment was performed using Multiwfn 3.8 dev software.[30] Visualization was carried out using VMD 1.9.3 software.[33] Molecules were randomly inserted into a cubic box according to specified ratios. Periodic boundary conditions were applied in the x, y, and z directions. Initial energy minimization was performed using the steepest descent method. The step size was set to 0.01 nm, and 10,000 iterations were conducted until the minimum force was less than 1.0 kJ·mol^{-1}·nm^{-1}, ensuring convergence. Van der Waals interactions were treated with a cutoff method. Electrostatic interactions were handled using the Particle Mesh Ewald (PME) method. The system was equilibrated at 1.0 bar pressure. Pressure control was managed by the Berendsen method. Temperature control was achieved using the V-rescale method. The time constant was set to 1.0 ps, and the compressibility was 4.5 × 10^{-5} bar^{-1}. The initial equilibration lasted 2000 ps with an integration time step of 0.002 ps. Pressure control was then switched to the Parrinello-Rahman method. NPT equilibration was extended to 10000 ps to obtain accurate box dimensions. During the equilibration phase, the system underwent 3000 ps of annealing. Gradual heating was applied to prevent instability. The final simulation ran for 60 ns. Trajectory files were output every 5000 steps. The LINCS algorithm was used to constrain hydrogen bonds.[34] Long-range dispersion corrections were applied to energy and pressure calculations. Trajectory files were analyzed post-simulation.

2D-HSQC NMR Characterization. Following our previously reported detection method[35,36], 2D-HSQC NMR and ^{31}P NMR analyses were performed separately. For 2D-HSQC NMR analysis, 20 mg of alkali lignin or pre-oxidized lignin was separately dissolved in 0.5 mL of DMSO-d_6. For ^{31}P NMR analysis, 20 mg of alkali lignin or pre-oxidized lignin was separately dissolved in 0.5 mL of phosphorylation reagent. The samples were then analyzed on an AVANCE III HD-500 (500 MHz) Bruker spectrometer.

For the NMR model study, CHPTAC was employed as a representative quaternary ammonium compound to mimic the cationic functionality of TEBAC, because both compounds contain a quaternary ammonium group, although their substituent structures are different. The CHPTAC-based model was therefore used to examine whether formic acid and a quaternary ammonium species would induce covalent grafting with lignin.

Field Emission Scanning Electron Microscopy (FE-SEM) Observation. Vacuum-dried lignin foam samples were cut into 5 × 5 × 5 mm cubes using a small bench saw. The samples were sputter-coated with Au/Pd and examined by FE-SEM at 5.0 kV under high vacuum mode for morphological observation. SEM images were processed using ImageJ software to analyze pore distribution, porosity, and average pore size.

Surface Area, Thermal, and Fire Performance. Specific surface area was determined by N_2 adsorption using the BET method, and pore structure parameters were obtained from the adsorption–desorption isotherms using the BJH model. Thermal conductivity was measured using a Hot Disk TPS2500S according to ISO 22007-2:2022. Combustion behavior was evaluated using cone calorimetry (ISO 5660–1, 35 kW m^{-2}). Compressive strength was measured following ASTM C365.

RESULTS AND DISCUSSION

Defining interaction density in the lignin–IAA system

To understand how supramolecular interactions govern material behavior in the lignin–IAA system, we first clarify the molecular origin and tunability of noncovalent interaction. As schematically defined in Figures 1A-B, this strategy avoids covalent modification of lignin and instead regulates intermolecular interactions through an interfacial amphiphilic agent (IAA) composed of FA and TEBAC. Interaction density is defined herein as an effective descriptor of the supramolecular interaction state within the lignin–IAA system rather than as an absolute material parameter. It encompasses the combined contributions of interaction-domain continuity, interaction strength, and the restric-

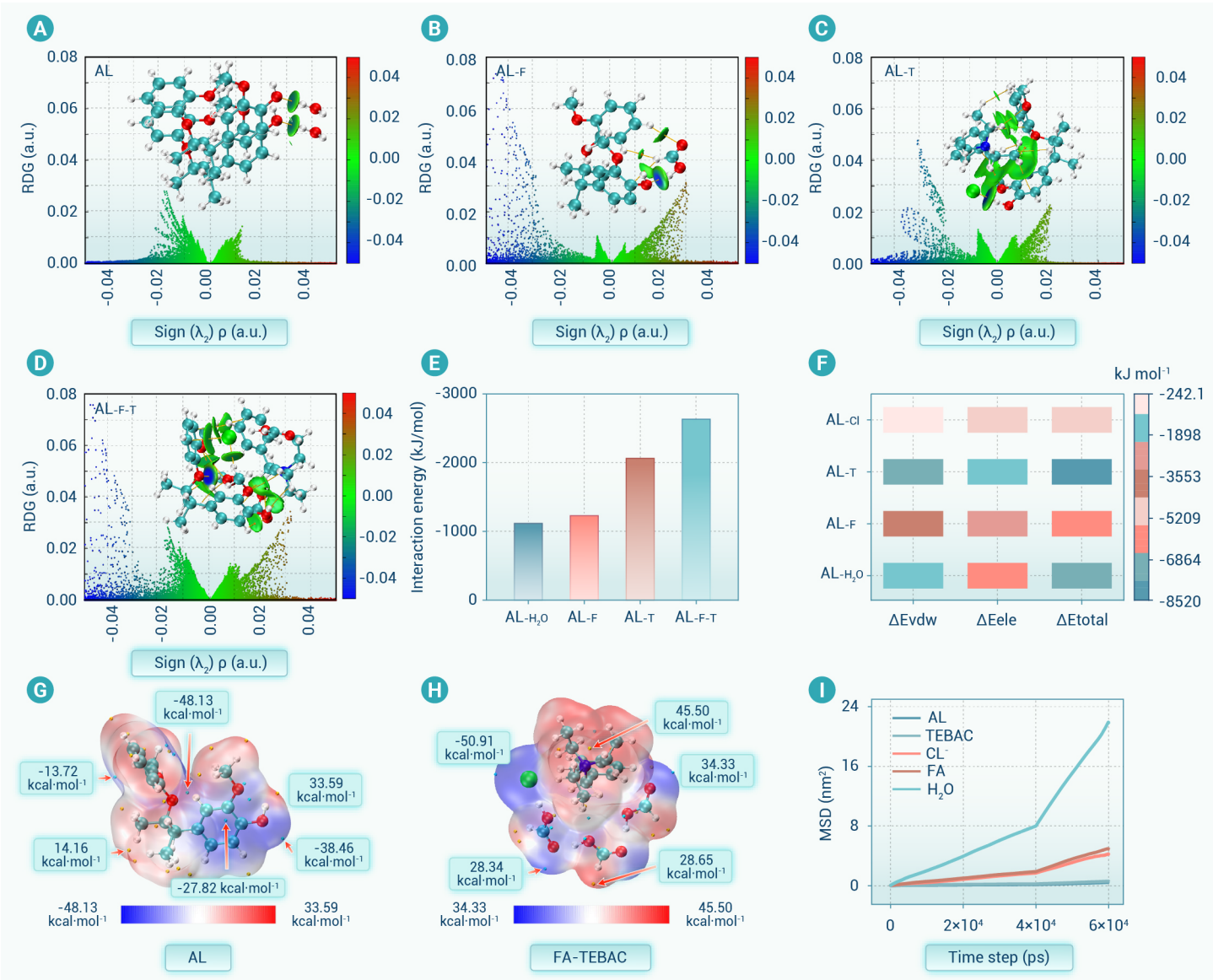


Figure 2. Molecular basis and tunability of interaction density in the lignin–IAA supramolecular system (A–D) Independent gradient model (IGM) analysis of noncovalent interactions in alkali lignin (AL) and its complexes with formic acid (FA), benzyltriethylammonium chloride (TEBAC), and their combination (FA–TEBAC). Pristine AL exhibits sparse and localized weak interactions, whereas the introduction of FA or TEBAC individually increases interaction regions through hydrogen bonding or electrostatic interactions, respectively. The combined FA–TEBAC system induces extensive and continuous interaction domains, indicating a pronounced enhancement in effective interaction density. (E) Calculated total interaction energies between lignin and different interaction partners, showing a systematic increase from pristine AL to AL–FA, AL–TEBAC, and AL–FA–TEBAC systems. (F) Decomposition of interaction energies into van der Waals and electrostatic contributions, highlighting the dominant role of electrostatic interactions in increasing interaction density upon FA–TEBAC incorporation. (G, H) Electrostatic potential (ESP) maps of AL and FA–TEBAC, illustrating the emergence of pronounced charge complementarity in the FA–TEBAC system that promotes stronger supramolecular interactions with lignin. (I) Mean square displacement (MSD) of lignin and small-molecule components, demonstrating that increased interaction density selectively suppresses lignin mobility while maintaining the dynamic nature of the supramolecular environment.

tion of lignin-chain mobility. These characteristics are evaluated through complementary analyses, including IGM characterization of noncovalent interaction domains, interaction-energy calculations, and analyses of lignin-chain mobility. Accordingly, interaction density is employed as a relative measure to compare variations in the supramolecular interaction state among different lignin–IAA systems and processing conditions.

At the molecular level, independent gradient model (IGM) analysis directly visualizes a stepwise amplification of interaction density upon IAA incorporation. In its pristine state, alkali lignin (AL) exhibits only sparse and localized weak interaction regions, reflecting predominantly intramolecular hydrogen bonding within its heterogeneous aromatic framework (Figure 2A).[37,38] Introducing FA or TEBAC individually increases the number of interaction regions (Figures 2B-C), but these domains remain fragmented and do not form a continuous interaction network across the lignin backbone. Strikingly, combining FA and TEBAC generates extensive and continuous interaction domains throughout the lignin structure (Figure 2D), indicating that cooperative hydrogen bonding and electrostatic interactions collectively enhance the effective interaction density beyond that achieved by either component alone.[39,40] This qualitative transition is further supported by single-component electrostatic analyses. COSMO σ-profiles show that AL and TEBAC share pronounced distributions in the nonpolar region (Figure S1), suggesting that TEBAC facilitates the dispersion and solubilization of lignin. ESP maps further reveal that both FA and TEBAC exhibit much stronger electrostatic heterogeneity than water, enabling charge-directed interaction (Figure S2).

These signatures are further supported by quantitative interaction energy analysis. Molecular dynamics calculations show that the total interaction energy between lignin and the IAA components increases systematically upon FA–TEBAC incorporation, exceeding those of the AL-FA and AL-TEBAC pairs (Figures 2E-F). Energy decomposition further shows that this enhancement is dominated by electrostatic interactions rather than van der Waals contacts (Figure 2F), consistent with the IGM observation of a more continu-

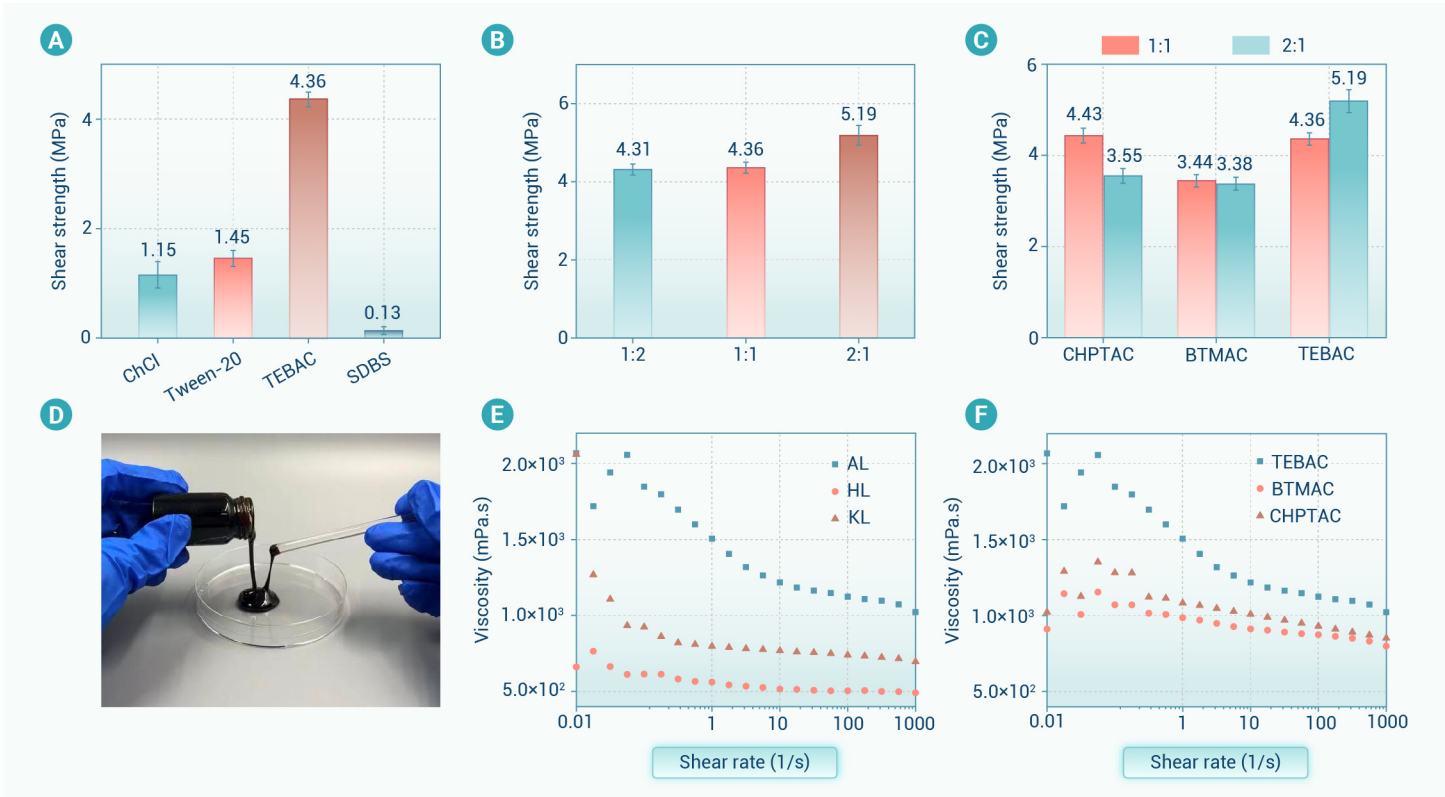


Figure 3. Adhesive-dominated solid state enabled by high interaction density in the lignin–IAA system (A) Comparison of lap shear strength of lignin-based adhesives formulated with different amphiphilic or ionic additives, highlighting the superior bonding performance achieved using benzyltriethylammonium chloride (TEBAC). (B) Effect of FA–TEBAC ratio on lap shear strength, demonstrating that high interaction density promotes adhesive performance. (C) Comparison of lap shear strength obtained using different quaternary ammonium salts at FA/amine ratios of 1:1 and 2:1, confirming the critical role of TEBAC in establishing a mechanically robust adhesive state. (D) Photograph showing the fluid processability of the supramolecular lignin adhesive prior to rapid interfacial locking. (E, F) Shear rate dependent viscosity of lignin adhesives prepared from different lignin sources (AL, HL, KL) and different quaternary ammonium salts, revealing pronounced shear thinning behavior and high zero shear viscosity indicative of supramolecular network formation under high interaction density.

ous interaction network when charge complementarity is maximized. Consistent with this mechanism, electrostatic potential mapping shows that while lignin exhibits heterogeneous surface potentials, the FA–TEBAC complex displays pronounced charge separation and complementary electrostatic regions (Figures 2G-H), providing a direct physical basis for programming interaction density through IAA composition rather than through chemical modification of the lignin backbone.[41,42] In addition, the IGM isosurface visualizations in Figure S3 further corroborate that distinct local interaction patterns arise depending on the interacting species (AL-H_2O, AL-F, AL-T, AL-Cl^-), supporting a chemically interpretable route to tune the interaction landscape.

To further characterize the short-range interaction structure, we analyzed radial distribution functions (RDFs). The RDF peak at r ≈ 2.05 Å between Cl^- (from TEBAC) and H (from FA) reveals a strong FA–TEBAC association motif (Figure S4A), suggesting the formation of ion-paired assemblies that can act as interfacial interaction mediators. A similarly pronounced peak at r ≈ 1.95 Å between O (from FA) and H (from AL) indicates strong FA–lignin hydrogen bonding (Figure S4C), showing that FA contributes direct hydrogen-bonding contacts with lignin, while TEBAC provides ionic interactions and dispersion assistance.[43,44] This behavior is consistent with the recognized acidity and hydrogen-bonding capability of FA in lignin processing and valorization.[45] Taken together, these RDF results support a cooperative interaction mechanism in which electrostatic interactions between Cl^- and quaternary ammonium groups promote lignin dispersion and strong ionic contacts, whereas FA provides directional hydrogen bonding.[46] The combined action of these interactions generates a denser and more continuous supramolecular interaction network than either component alone.

If interaction density changes meaningfully in the lignin–IAA system, corresponding constraints on polymer mobility should be measurable. Diffusion and mean square displacement analyses clearly capture this effect. As interaction density increases, lignin diffusion is selectively suppressed (diffusion coefficient decreases from ~ 0.08 to < 0.05 $nm^2\ ps^{-1}$; Figure 2I and Table S2), whereas small-molecule components remain comparatively mobile. This selective immobilization indicates that the supramolecular network forms primarily on the lignin scaffold, effectively locking lignin within a mechanically coherent interaction network while preserving a dynamic microenvironment, a condition that enables access to divergent material states through processing (Figure 1B).[47] Critically, multiple spectroscopic and structural characterizations confirm that these changes arise from supramolecular regulation rather than covalent chemistry. 2D-HSQC NMR spectra reveal no new covalent cross-peaks attributable to grafting reactions (Figure S5).[48] The FTIR results indicate that the characteristic structural features of lignin are largely retained, with no obvious emergence of new absorption bands associated with major chemical transformation (Figure S6). XRD patterns remain broadly amorphous and show no evidence of new crystalline phases (Figure S7), and XPS C1s spectra show comparable carbon-speciation distributions across AL, AL-F, AL-T, and AL-F-T (Figure S8). Together, these results show that interaction density can be systematically tuned without modifying the lignin backbone and can therefore be used to interpret how the same lignin platform is directed toward different material states.[49]

A high interaction density regime enables an adhesive dominated state

At sufficiently high interaction density, supramolecular interactions in the lignin–IAA system percolate into a continuous network that supports mechanical integrity and enables rapid interfacial locking at room temperature, consistent with the supramolecular adhesion mechanism reported in previous studies.[50,51] Consequently, the system forms an adhesive-dominated solid state that combines short-time processability with strong ambient bonding (Figures 1A-B).

The macroscopic consequence of this interaction regime is reflected in the measured adhesion performance. A broad additive screening shows that lignin components deliver the highest lap shear strength when TEBAC serves

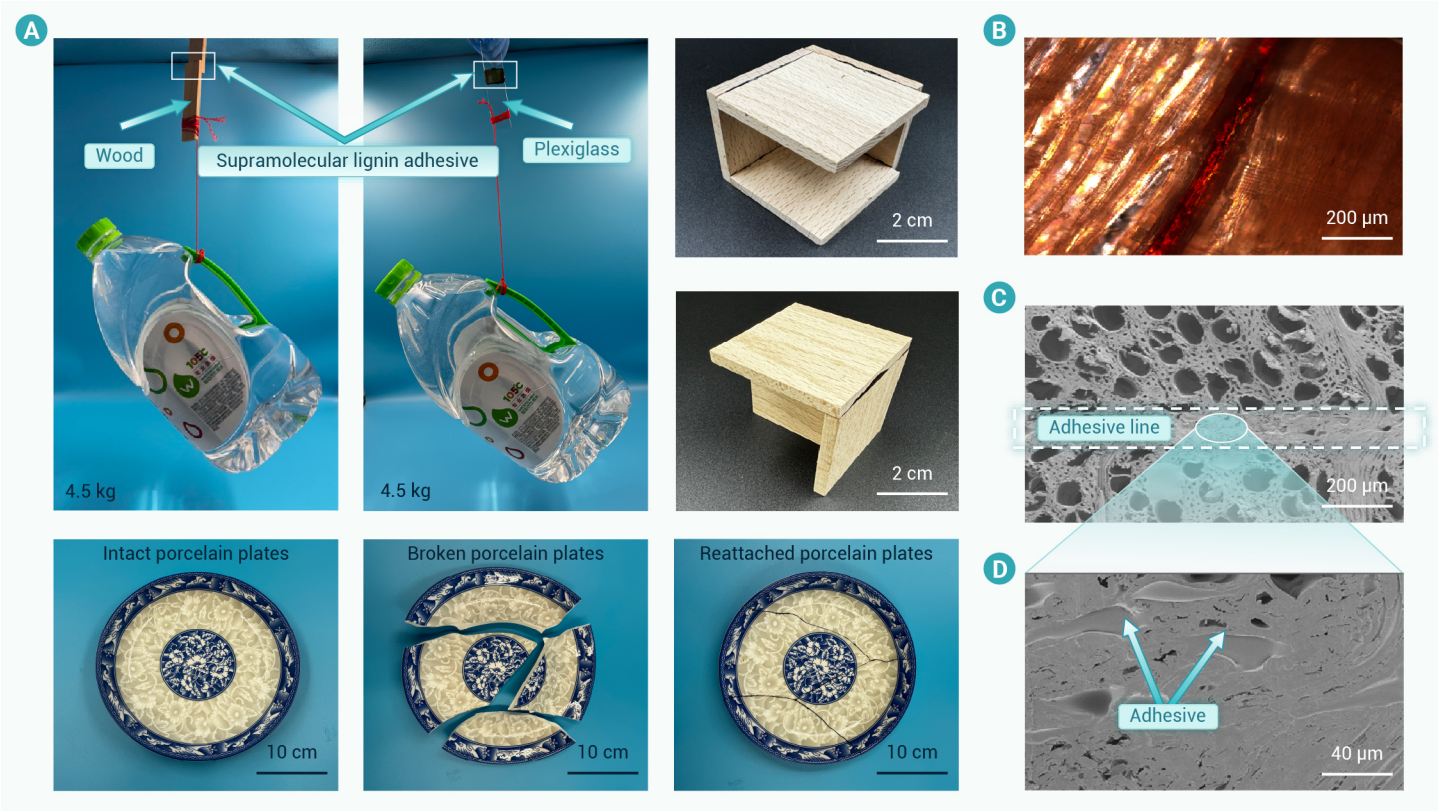


Figure 4. Practical bonding demonstrations and adhesive–wood interfacial structure (A) Demonstration of the strong adhesive-dominated state, including load-bearing tests on wood and plexiglass substrates (4.5 kg), repair of a fractured porcelain plate, and fabrication of load-bearing wooden components using the supramolecular lignin adhesive. (B) Optical microscopy image of the adhesive–wood interface, showing intimate interfacial contact. (C, D) SEM images of the adhesive layer and interfacial region, revealing a continuous adhesive phase and effective penetration into the porous wood substrate, consistent with a mechanically integrated adhesive interphase.

as the quaternary ammonium component, outperforming other amphiphilic or ionic additives (Figure 3A). Further systematic variation of the FA–TEBAC composition reveals a strong composition dependence, with an optimized FA–TEBAC ratio producing a maximum lap shear strength of 5.19 MPa for the AL-based adhesive under ambient curing conditions (Figure 3B). The applicability of this supramolecular adhesion strategy to structurally distinct industrial lignins was further evaluated using AL, HL, and KL, among which the KL-based adhesive achieved the highest lap shear strength of 5.46 ± 0.12 MPa (Figure S9E). In contrast, alkali lignin exhibits negligible adhesion (< 0.5 MPa), indicating that strong bonding is not an intrinsic characteristic of lignin but the result of strengthened supramolecular interactions at high interaction density. Importantly, substituting TEBAC with other quaternary ammonium salts while maintaining identical FA/amine ratios (1:1 and 2:1) results in substantially reduced bonding strength (Figure 3C), demonstrating that the adhesive-dominated state is not simply induced by ionic additives in general but requires the specific interaction environment created by the FA–TEBAC pair.

Crucially, the adhesive-dominated state forms while maintaining practical processability.[52] The lignin–IAA formulation remains fluid during application, allowing effective spreading and wetting of the substrates before locking into place (Figure 3D). Rheological measurements provide direct evidence for the formation of a supramolecular solid under high interaction density. Specifically, the viscosity measured over a range of shear rates exhibits pronounced shear thinning and a high zero-shear viscosity, suggesting the presence of a physically percolated interaction network (Figures 3E-F).[53] Notably, this viscoelastic signature is observed across adhesives prepared from different lignin sources (AL, HL, KL) as well as across different quaternary ammonium salt variants (Figures 3E-F). These results show that while the FA–TEBAC pair provides the highest bonding strength (Figures 3A-C), the formation of a solid-like supramolecular network under high interaction density is a general phenomenon rather than a source-specific artifact. This general behavior is also observed at the joint level. Lap shear tests on wood joints prepared from AL, HL, and KL show consistently strong bonding when processed under the adhesive state conditions (Figure S9E). The lap shear setup and specimen geometry used for these measurements are shown in Figures S9C & S11 to ensure reproducibility and to align the reported strength values with standard testing practice. Finally, three-dimensional reconstructed images confirm that the adhesive-dominated state forms a continuous and homogeneous internal structure when FA and TEBAC are combined, whereas systems lacking either component display discontinuous or heterogeneous morphologies (Figure S10).

The lignin–IAA adhesive also shows reliable performance in practical bonding scenarios. Demonstrations such as load-bearing tests on wood and plexiglass substrates supporting 4.5 kg, repair of fractured porcelain plates, and fabrication of load-bearing wooden components demonstrate rapid ambient bonding and mechanical reliability in representative scenarios (Figure 4A). Optical microscopy shows intimate contact across the adhesive wood interface without obvious interfacial voids (Figure 4B). Further evidence from SEM imaging shows a continuous adhesive phase and effective penetration into the porous wood microstructure, which forms a mechanically integrated interphase (Figures 4C-D).[54] This penetration and interlocking behavior is further illustrated schematically and supported by cross-sectional microstructural evidence in Figures S9A-B & D. These results indicate that the supramolecular lignin network infiltrates the wood porosity before rapid solidification, enabling efficient stress transfer during lap shear loading.

Overall, high interaction density leads the lignin–IAA system to form a distinct adhesive-dominated solid state. This state acts as the adhesive interlayer that enables subsequent spatial coupling with the porous architecture derived from the same lignin platform. In addition to its strong dry-state bonding performance, the lignin–IAA adhesive shows room-temperature processability and a simple supramolecular regulation pathway without covalent modification of the lignin backbone. These features allow the adhesive state and porous state to be integrated within the same lignin–IAA system. However, because the interfacial locking is mainly governed by dynamic hydrogen-bonding and electrostatic interactions, the current adhesive network is sensitive to water exposure and its long-term environmental

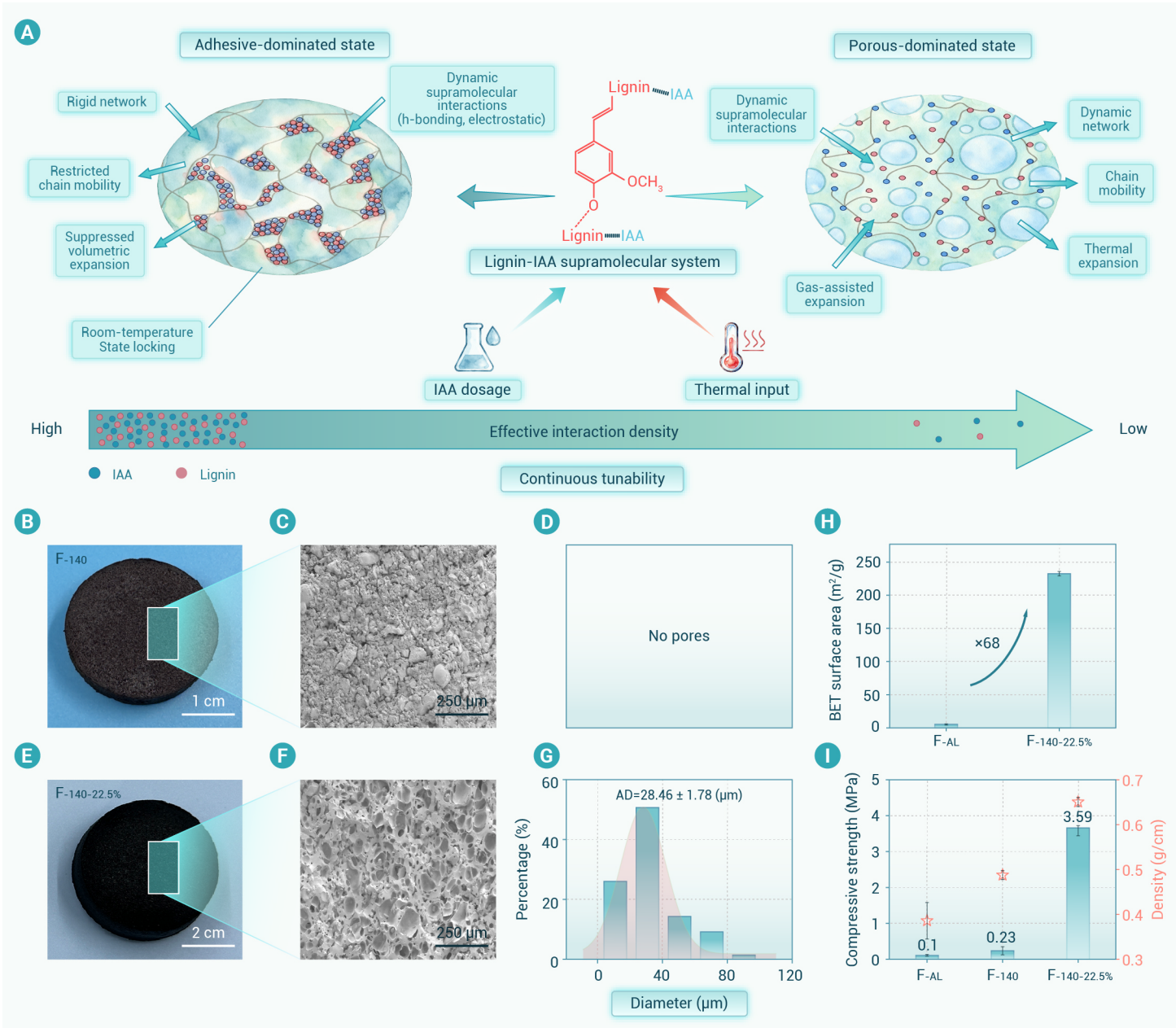


Figure 5. Reduced effective interaction density redirects the lignin–IAA system toward porous architectures (A) Schematic illustration of the development of porous architectures under reduced effective interaction density in the lignin–IAA system. Reducing effective interaction density through chemical pre-oxidation and controlled IAA incorporation prevents excessive hydrogen-bond-induced network rigidification, restores chain mobility and gas diffusion under thermal input, and thereby enables gas-assisted expansion and the formation of a porous-dominated architecture. (B–D) Lignin-based materials prepared from pre-oxidation alkali lignin without IAA (F-140) after thermal treatment, showing limited volumetric expansion and a compact, nonporous morphology, indicating that interaction density is reduced but remains above the threshold required for pore stabilization. (E, F) Lignin-based foam prepared from pre-oxidation alkali lignin with 22.5 wt% IAA (F-140-22.5%), exhibiting substantial volumetric expansion and a well-developed porous architecture, demonstrating that further reduction and redistribution of interaction density enable a stable porous-dominated architecture. (G) Pore size distribution of the porous-dominated state (F-140-22.5%), revealing an average pore diameter of 28.46 ± 1.78 μm. (H) BET specific surface area comparison, showing a pronounced increase upon the formation of the porous-dominated state, reflecting the formation of interconnected pore networks. (I) Compressive strength and bulk density of F-AL, F-140, and F-140-22.5% prepared under different interaction-regulation conditions, showing the evolution of mechanical properties and bulk density during the transition toward the porous-dominated state. F-140-22.5% exhibits a bulk density of 0.65 g cm^{-3} and a compressive strength of 3.59 MPa.

durability still requires further improvement. Therefore, the present system is more suitable for dry-state bonding or potentially reversible adhesion at this stage, while further hydrophobic regulation or network-stabilization strategies may improve its wet-state performance and durability.

Reduced effective interaction density redirects the system toward porous architectures

In contrast to the adhesive-dominated regime, reducing the effective interaction density redirects the lignin–IAA system toward a porous architecture by establishing a suitable supramolecular and rheological window for thermally driven matrix expansion and pore-wall stabilization, rather than acting as the direct origin of pore generation. Importantly, the formation of porosity does not arise from network collapse or macroscopic phase separation. Instead, it results from a redistribution of the balance between supramolecular cohesion and chain mobility during thermal activation, which enables gas-assisted expansion within a still connected framework (Figure 5A).[55] Access to this porous-dominated state strongly depends on the molecular structure of lignin prior to the foaming process. Controlled pre-oxidation systematically adjusts the distribution of functional groups in lignin while maintaining the integrity of the aromatic backbone. This adjustment lowers the upper limit of attainable interaction density and prevents excessive rigidification during thermal treatment.[56,57]

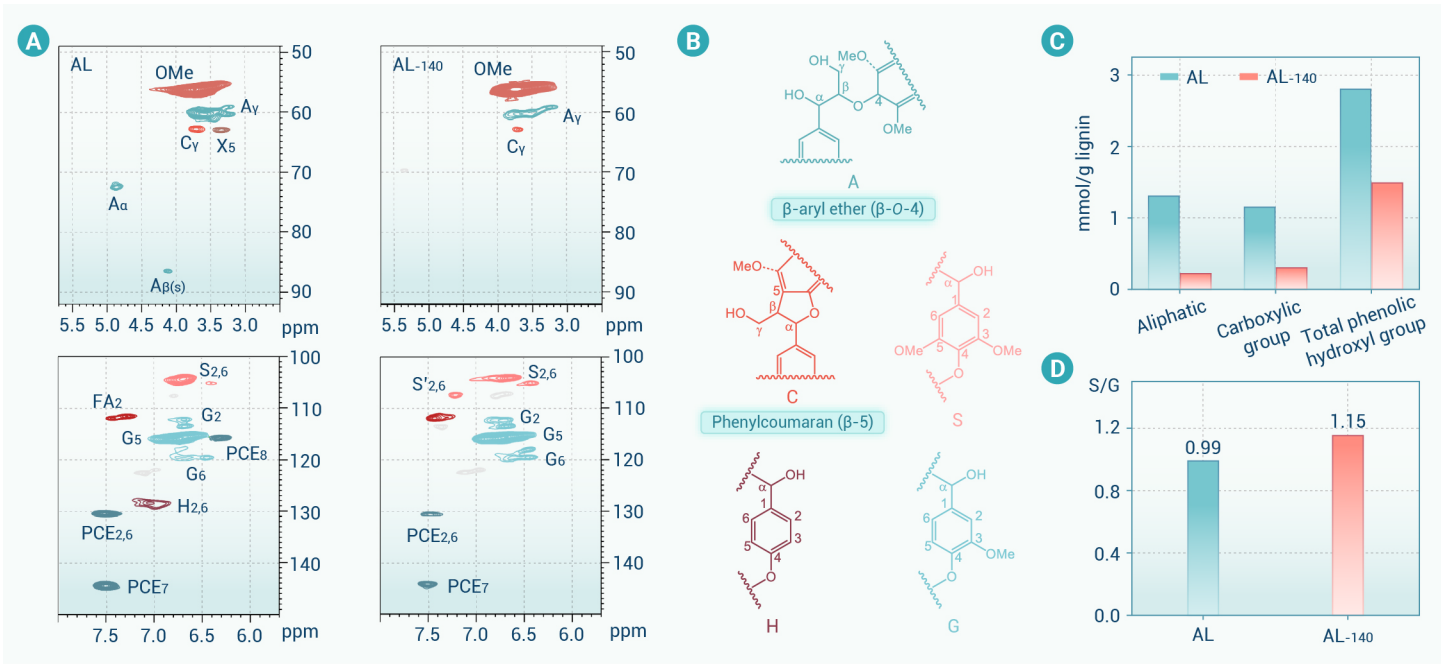


Figure 6. Structural evolution of lignin during pre-oxidation (A) 2D-HSQC NMR spectra of alkali lignin (AL) and pre-oxidized lignin (AL-140), indicating that pre-oxidation modifies the functional-group distribution without disrupting the aromatic backbone. (B) Assignments of representative lignin substructures used for HSQC analysis. (C) Quantitative comparison of the aliphatic hydroxyl, carboxyl, and total phenolic hydroxyl contents, showing that pre-oxidation selectively suppresses excessive interaction sites and lowers the effective interaction density. (D) Syringyl-to-guaiacyl (S/G) ratios of AL and AL-140, confirming that interaction-density regulation is achieved through functional-group redistribution rather than fundamental compositional change.

Within this interaction-density window, the system exhibits a threshold-controlled morphological response.[58] These observations indicate that pore formation requires a balanced interaction-density regime that enables expansion while maintaining pore-wall stability. When pre-oxidized lignin is thermally treated without the addition of IAA, the resulting material exhibits only limited volumetric expansion and remains compact and nonporous (Figures 5B-D). This result indicates that pre-oxidation alone reduces excessive hydroxyl-mediated interactions, but the system still does not reach the balanced interaction-density state required for gas-assisted pore formation. By contrast, introducing 22.5 wt% IAA into the pre-oxidized lignin system further redistributes supramolecular interactions and provides sufficient molecular mobility under thermal activation, inducing substantial expansion and producing a well-developed porous architecture (Figures 5E-F). Additional morphological observations presented in Figure S16 provide further evidence for this interpretation. Non-pre-oxidized lignin without IAA expands in an uncontrolled manner and forms irregular pores, whereas pre-oxidized lignin without IAA remains compact and essentially nonporous. When IAA is introduced into the pre-oxidized lignin system, the material develops a uniform and interconnected porous structure. Therefore, pore formation is not a simple consequence of lowering interaction density or thermal treatment alone, but results from tuning interaction density into a balanced regime that couples chain mobility, gas diffusion, and pore-wall stabilization. While the present results highlight the important role of interaction-density regulation in porous-architecture formation, the foaming process is likely associated with the coupled effects of thermally induced volatile release, matrix expansion, and supramolecular stabilization. Accordingly, the proposed mechanism provides a conceptual framework for understanding how interaction-density regulation modulates pore development and stabilization in the lignin–IAA system.

Once the system reaches a porous-dominated state, its porous architecture becomes both quantifiable and tunable. F-140-22.5% exhibits a narrow pore size distribution, with an average pore diameter of 28.46 ± 1.78 μm (Figure 5G), indicating that pore formation is well regulated rather than arising from stochastic void generation. Consistently, when the system transforms into a porous state, the BET specific surface area increases significantly (Figure 5H). This result is also consistent with the BET trends observed at different IAA contents, as summarized in Figure S17A. Importantly, systematic regulation of the IAA content leads to continuous increases in both macroscopic expansion and pore size (Figure S18), indicating that the porous-dominated state is tunable. In this process, interaction density serves as the key parameter governing pore architecture and accessible surface area.

A critical hallmark of this structural evolution is that the porous architecture develops while mechanical integrity is markedly enhanced. The compressive-strength–density relationship of F-AL, F-140, and F-140-22.5% prepared under different interaction-regulation conditions shows a pronounced increase in compressive strength during the transition toward the porous-dominated state (Figure 5I).[59] In particular, F-140-22.5% exhibits a bulk density of 0.65 g cm^{-3} and a compressive strength of 3.59 MPa, indicating the formation of a continuous load-bearing framework. This trend is further supported by the broader dataset in Figure S17B, which shows the relationships between compressive strength and density, as well as between porosity and mechanical properties. These results suggest that adjusting the interaction density enables a predictable balance between structure and properties, rather than merely producing fragile porous structures. The pressure forming setup and mold used to prepare consistent precursors for foam fabrication are documented in Figure S12, ensuring that the observed structural evolution reflects interaction-density regulation rather than uncontrolled specimen geometry. The oxidation temperature series reveals progressive variations in lignin appearance, thermal evolution behavior, and FTIR spectra (Figure S13).

2D-HSQC analysis further indicates gradual structural evolution in lignin subunits across increasing oxidation conditions (Figure S14). Quantitative hydroxyl analysis shows that pre-oxidation selectively reduces excessive interaction sites by decreasing the contents of aliphatic and phenolic hydroxyl groups (Figure S15). A direct comparison of AL and lignin pre-oxidized at 140°C (AL-140) in Figure 6A, interpreted using the representative structural assignments shown in Figure 6B, demonstrates that pre-oxidation modifies the distribution of lignin functional groups without disrupting the fundamental aromatic backbone. Quantitative functional-group analysis shows decreases in the aliphatic and phenolic hydroxyl contents following pre-oxidation (Figures 6C-S15), indicating a reduction in interaction-relevant sites

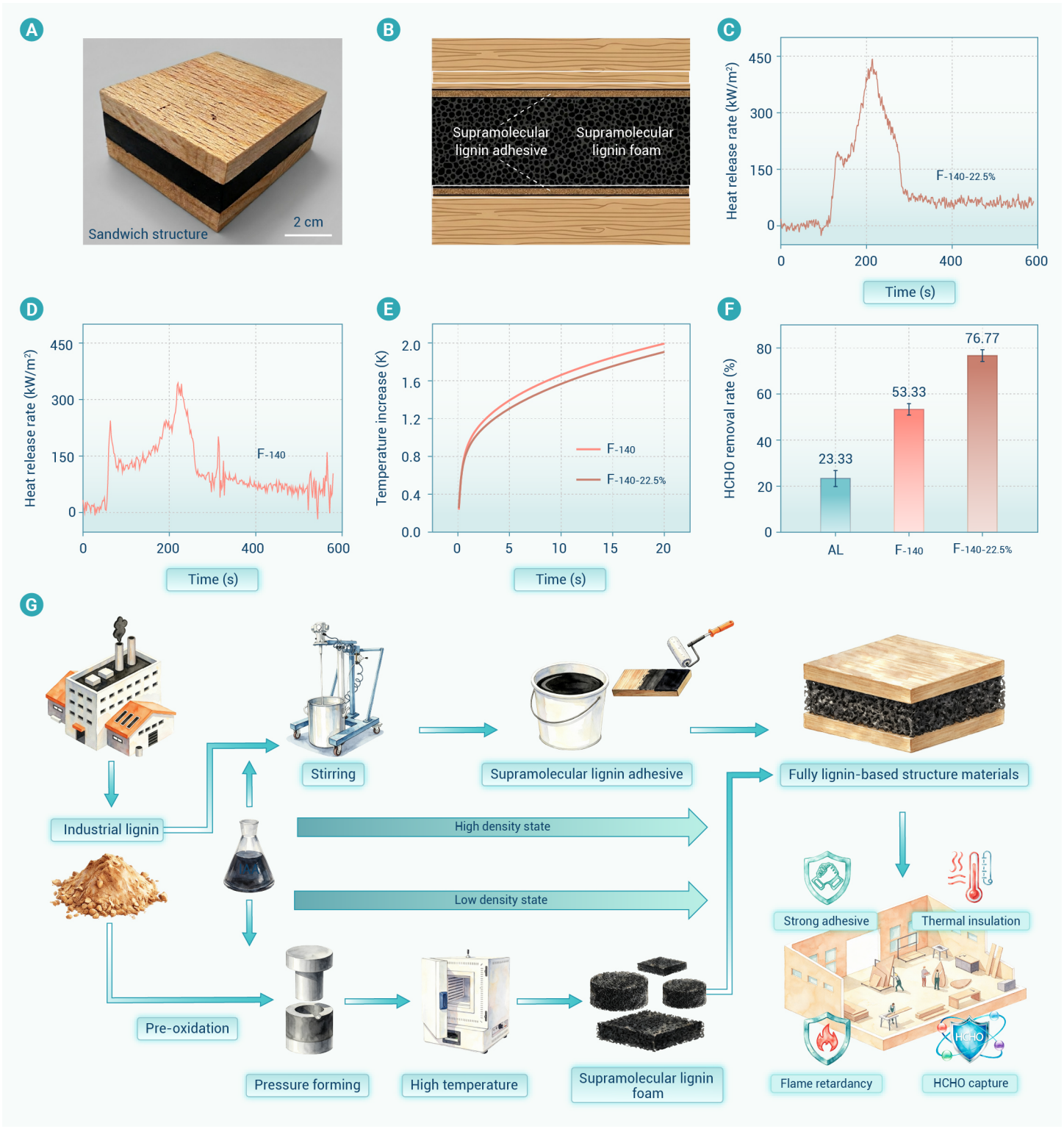


Figure 7. Integration of adhesive- and porous-dominated states into sandwich composite structures with multifunctionality (A) Photograph of a sandwich composite constructed by spatially coupling adhesive- and porous-dominated states derived from the same supramolecular lignin system with wood veneers. (B) Schematic cross-sectional illustration of the sandwich architecture, in which the supramolecular lignin adhesive serves as the adhesive interlayer, while the supramolecular lignin foam functions as the multifunctional core between wood veneer facings. (C, D) Heat release rate curves of lignin-based foams prepared under reduced interaction density conditions with (F-140-22.5%) and without (F-140) IAA, demonstrating enhanced flame retardancy upon formation of the porous-dominated state. (E) Transient temperature increase measured on the cold side of lignin-based materials, showing improved thermal insulation performance for the porous-dominated state (F-140-22.5%) compared with the non-porous counterpart (F-140). (F) HCHO removal efficiency of alkali lignin (AL), pre-oxidized lignin foam without IAA (F-140), and porous-dominated lignin foam with IAA (F-140-22.5%), highlighting the multifunctional adsorption capability enabled by the porous architecture. (G) Schematic overview of the interaction-density-directed supramolecular engineering strategy, illustrating how industrial lignin is directed into adhesive- or porous-dominated states under high- and low-interaction-density conditions, respectively, and subsequently assembled with wood veneers into sandwich composite structures integrating strong adhesion, thermal insulation, flame retardancy, and HCHO capture.

while preserving the fundamental lignin framework. The comparison of syringyl-to-guaiacyl ratios in Figure 6D further supports that this regulation originates primarily from functional-group redistribution rather than a fundamental change in aromatic-unit composition. Together, these results identify

pre-oxidation as a molecular-level control step that shifts the lignin–IAA system into an interaction-density range suitable for thermally driven expansion and stable pore formation.

Functional role of the porous foam core in integrated composite structures

Beyond structural formation, the porous-dominated state generated through interaction density reduction is intentionally designed to function as an active core in integrated composite architectures rather than as an isolated foam. As shown in Figures 7A-B, the porous lignin core can be combined with wood veneers and adhesive interlayers derived from the same lignin–IAA system to form a sandwich composite structure. In this configuration, the porous framework serves as a functional component whose pore structure and physicochemical properties contribute to thermal insulation, fire resistance, and environmental adsorption performance.[60] Because both components originate from the same supramolecular system, good interfacial compatibility is achieved, and no obvious delamination or interfacial defects are observed.

Within this integrated design, the porous-dominated state exhibits pronounced flame-retardant behavior. Cone calorimetry tests show delayed ignition and altered heat-release behavior after porous architecture formation (Figures 7C-D). In particular, the porous sample exhibits an ignition time of 53 s, indicating improved resistance to ignition after porous architecture formation. These results suggest that F-140-22.5% exhibits flame-retardant behavior approaching the performance level generally associated with GB 8624 B1 materials.[61] The enhanced flame retardancy originates from the combined effects of the aromatic lignin framework and the porous architecture.[62] During combustion, the aromatic structure facilitates char formation, while the porous structure limits heat and mass transfer. As a result, the material exhibits improved flame-retardant performance without the need for external flame-retardant additives. The porous-dominated state also provides effective thermal insulation. As shown in Figure 7E, F-140-22.5% exhibits a smaller cold-side temperature increase than F-140, demonstrating improved thermal-insulation performance.[63] The thermal conductivity of the porous sample reaches 0.128 W m^{-1} K^{-1}, confirming its effectiveness as a lightweight insulating core. Although this value does not match that of commercial extruded polystyrene insulation foam[64], the fully biomass-derived rigid foam still exhibits practical thermal-insulation capability and can be used as an insulating filler in building interiors or as an insulating layer in furniture structures. This thermal insulation behavior results from the combined effect of air-filled pores and the inherently low thermal diffusivity of the lignin matrix. These results demonstrate that porosity generated through interaction density regulation provides an effective strategy for producing lightweight insulating cores without the need for foreign fillers or polymeric foams. In addition, the porous-dominated state provides effective environmental adsorption capability. Owing to its high specific surface area and accessible pore network, the porous lignin framework enables efficient uptake of small molecules.[65] HCHO adsorption experiments show rapid kinetics and higher HCHO removal efficiency than compact lignin materials (Figure 7F). The porous sample reaches an HCHO removal efficiency of 76.77%, highlighting the functional advantage introduced by pore formation. This is particularly meaningful because many conventional wood-based composites are formaldehyde sources, whereas the present material can actively remove HCHO. This behavior correlates with the pore architecture generated through interaction density regulation, as supported by the systematic evolution of pore size and surface area in Figures S16-S18. The results indicate that the pore structure is generated under this interaction regime rather than by post-synthetic surface modification.

Overall, the multifunctionality of the sandwich composite arises from the spatial integration of the adhesive-dominated and porous-dominated states within the same lignin–IAA platform. The adhesive-dominated interlayer enables effective assembly between the wood veneers and the porous lignin core, while the interconnected pore network and lignin-rich framework contribute to thermal insulation, flame-retardant behavior, and formaldehyde adsorption. Rather than serving as a fully optimized structural panel, this sandwich structure is presented as a proof-of-concept demonstration of how interaction-density-directed supramolecular engineering can organize different lignin-derived material states into an integrated multifunctional architecture. This concept provides a useful design perspective for the future development of lignin-based composite materials in which adhesion, porosity, and functionality can be coupled within a unified material platform. The overall strategy for directing lignin into distinct material states and integrating them within a multifunctional sandwich architecture is summarized schematically in Figure 7G.

CONCLUSION

In summary, this work demonstrates that tuning supramolecular interactions in a lignin–IAA system enables access to both adhesive-dominated and porous material states from a common lignin platform. Under high interaction density, the lignin network develops into a mechanically coherent adhesive state that supports rapid room temperature bonding with lap shear strengths up to 5.46 MPa. When the effective interaction density is adjusted into a balanced pore-forming window through pre-oxidation and controlled IAA incorporation, the same system is redirected toward a porous architecture. The representative F-140-22.5% foam exhibits a density of 0.65 g cm^{-3}, a compressive strength of 3.59 MPa, and a specific surface area above 230 m^2/g. Because both the adhesive and porous components originate from the same lignin-based supramolecular system, they can be assembled with wood veneers into an integrated sandwich composite, in which the porous foam core provides thermal insulation (0.128 W m^{-1} K^{-1}), flame retardancy (ignition time of 53 s), and HCHO removal (76.77%), while the adhesive interlayers ensure structural integrity. More broadly, this work highlights a supramolecular route for linking material state, architecture, and function in lignin-based systems, and provides a practical strategy for developing multifunctional composite materials from renewable feedstocks.

REFERENCES

1. Bechthold M. and Weaver J. C. (2017). Materials science and architecture. *Nat. Rev. Mater.* **2**:17082. DOI:10.1038/natrevmats.2017.82
2. An L., Guo Z., Li Z., et al. (2022). Tailoring thermal insulation architectures from additive manufacturing. *Nat. Commun.* **13**:4309. DOI:10.1038/s41467-022-32027-3
3. Zhang Y., Liu Y., Ren G., et al. (2025). High-throughput printing of functionally gradient material from self-propagation. *Nat. Commun.* **16**:9706. DOI:10.1038/s41467-025-65189-x
4. Hayes G., Laurel M., MacKinnon D., et al. (2023). Polymers without petrochemicals: Sustainable routes to conventional monomers. *Chem. Rev.* **123**:2609–2734. DOI:10.1021/acs.chemrev.2c00354
5. Cavalcante J., Oldal D. G., Peskov M. V., et al. (2024). Biobased interpenetrating polymer network membranes for sustainable molecular sieving. *ACS Nano* **18**:7433–7443. DOI:10.1021/acsnano.3c10827
6. Weyhrich C. W., Petrova S. P., Edgar K. J., et al. (2023). Renewed interest in biopolymer composites: Incorporation of renewable, plant-sourced fibers. *Green Chem.* **25**:106–129. DOI:10.1039/d2gc03384d
7. Seidi F., Liu Y., Huang Y., et al. (2025). Chemistry of lignin and condensed tannins as aromatic biopolymers. *Chem. Soc. Rev.* **54**:3140–3232. DOI:10.1039/d4cs00440j
8. Sun R. C. (2020). Lignin source and structural characterization. *ChemSusChem* **13**:4385–4393. DOI:10.1002/cssc.202001324
9. Yan L., Huertas-Alonso A. J., Liu H., et al. (2025). Lignin polymerization: Towards high-performance materials. *Chem. Soc. Rev.* **54**:6634–6651. DOI:10.1039/d4cs01044b
10. Sulis D. B., Lavoine N., Sederoff H., et al. (2025). Advances in lignocellulosic feedstocks for bioenergy and bioproducts. *Nat. Commun.* **16**:1244. DOI:10.1038/s41467-025-56472-y
11. Liu R. Y., Li B. Z., Yuan Y. J., et al. (2025). Multiscale metabolic engineering in biological lignin valorization. *The Innovation* **6**:100993. DOI:10.1016/j.xinn.2025.100993
12. Zhang B., Qiang G., Barta K., et al. (2024). Bio–based polymers from lignin. *Innov. Mater.* **2**:100062. DOI:10.59717/j.xinn-mater.2024.100062
13. Pang T., Wang G., Sun H., et al. (2021). Lignin fractionation: Effective strategy to reduce molecule weight dependent heterogeneity for upgraded lignin valorization. *Ind. Crop. Prod.* **165**:113442. DOI:10.1016/j.indcrop.2021.113442
14. Upton B. M. and Kasko A. M. (2016). Strategies for the conversion of lignin to high-value polymeric materials: Review and perspective. *Chem. Rev.* **116**:2275–2306. DOI:10.1021/acs.chemrev.5b00345
15. Shanker R., Mao A., Liu L., et al. (2025). Structurally colored thin films based on acetylated lignin nanoparticles. *ACS Nano* **19**:24713–24723. DOI:10.1021/acsnano.4c16679
16. Liu T., Xue W., Liu Y., et al. (2026). Cellulose - tannin - glycerol (CTG): A biomass - based, recyclable, and high - performance adhesive via water - regulated cohesion. *Adv. Funct. Mater.* **36**:2532068. DOI:10.1002/adfm.202532068
17. Gong Z., Yang G., Wu T., et al. (2026). Screening high-quality lignins extracted from biomass to prepare biobased wood adhesives. *Nat. Protoc.* **21**:3614–3641. DOI:10.1038/s41596-025-01316-8
18. Liu K., Kang Y., Wang Z., et al. (2013). 25th anniversary article: reversible and adaptive

functional supramolecular materials: "noncovalent interaction" matters. *Adv. Mater.* **25**:5530–5548. DOI:10.1002/adma201302015
19. Zheng N., Xu Y., Zhao Q., et al. (2021). Dynamic covalent polymer networks: A molecular platform for designing functions beyond chemical recycling and self-healing. *Chem. Rev.* **121**:1716–1745. DOI:10.1021/acs.chemrev.0c00938
20. Zhan B., Zhang L., Deng Y., et al. (2023). A multifunctional lignin-based composite ultra-adhesive for wood processing. *Green Chem.* **25**:10061–10071. DOI:10.1039/d3gc03542e
21. Liu Q., Wang Y., Wang H., et al. (2023). Fluidic lignin with ultra-low glass transition temperature (Tg < −57 °C): a versatile polyelectrolyte solvent platform. *Green Chem.* **25**:5142–5149. DOI:10.1039/d3gc01248d
22. Zhang L., Sun Y., Huang S., et al. (2025). Poly(acrylic acid)-grafted cellulose nanocrystal reinforced supramolecular adhesives: Ultrahigh strength, humidity resistance, and pH-controlled recyclability. *Carbohydr. Polym.* **363**:123705. DOI:10.1016/j.carbpol.2025.123705
23. Wu T., Jia Z., Meng Y., et al. (2025). Biomass-based strong adhesive based on supramolecular deep eutectic solvents pretreatment. *Chem. Eng. J.* **505**:159055. DOI:10.1016/j.cej.2024.159055
24. Lin H. Y., Li L., Zhang Q., et al. (2025). Robust supramolecular adhesives based on natural small molecules through hydrogen bonding. *Chem.-Eur. J.* **31**:e202500900. DOI:10.1002/chem.202500900
25. Zhang J., Wang W., Zhang Y., et al. (2022). Small-molecule ionic liquid-based adhesive with strong room-temperature adhesion promoted by electrostatic interaction. *Nat. Commun.* **13**:5214. DOI:10.1038/s41467-022-32997-4
26. Xie X., Jiang Y., Yao X., et al. (2024). A solvent-free processed low-temperature tolerant adhesive. *Nat. Commun.* **15**:5017. DOI:10.1038/s41467-024-49503-7
27. Lei Z., Shao J., Li C., et al. (2025). Skin - Inspired durable and cost - effective biomass - based supramolecular adhesives. *Adv. Funct. Mater.* **35**:2501624. DOI:10.1002/adfm.202501624
28. Ju H., Yin Z., Demchuk Z., et al. (2024). Constructing crown ether - based supramolecular adhesives with ambient - temperature applicable and durable adhesion. *Adv. Funct. Mater.* **34**:2402165. DOI:10.1002/adfm.202402165
29. Neese F. (2012). The ORCA program system. *Wiley Interdiscip. Rev. Comput. Mol. Sci* **2**:73–78. DOI:10.1002/wcms.81
30. Lu T. and Chen F. (2012). Multiwfn: A multifunctional wavefunction analyzer. *J. Comput. Chem* **33**:580–592. DOI:10.1002/jcc.22885
31. Lu T. and Chen Q. (2021). Interaction region indicator: A simple real space function clearly revealing both chemical bonds and weak interactions. *Chem. Methods* **1**:231–239. DOI:10.1002/cmtd.202100007
32. Abraham M. J., Murtola T., Schulz R., et al. (2015). GROMACS: High performance molecular simulations through multi-level parallelism from laptops to supercomputers. *SoftwareX* **1-2**:19–25. DOI:10.1016/j.softx.2015.06.001.
33. Humphrey W., Dalke A., and Schulten K. (1996). VMD: Visual molecular dynamics. *J. Mol. Graph* **14**:33–38. DOI:10.1016/0263-7855(96)00018-5
34. Hess B., Bekker, H., Berendsen, H.J.C., and Fraaije, J.G.E.M. (1997). LINCS: A linear constraint solver for molecular simulations. *J. Comput. Chem* **18**:1463–1472. DOI:10.1002/(SICI)1096-987X(199709)18:12<1463::AID-JCC4>3.0.CO;2-H
35. Wen J.-L., Yuan T.-Q., Sun S.-L., et al. (2014). Understanding the chemical transformations of lignin during ionic liquid pretreatment. *Green Chem.* **16**:181–190. DOI:10.1039/c3gc41752b
36. Zuo C., Hui X.-Y., Xin P.-A., et al. (2026). A green one-pot strategy for sustainable fully lignin-based adhesives. *Green Chem.* **28**:974–985. DOI:10.1039/d5gc05305f
37. Yi L., Luo D., Feng M., et al. (2026). Unraveling molecular interactions in coal-derived phenolic–aromatic systems: A decoupling principle governing assembly. *Fuel* **413**:138232. DOI:10.1016/j.fuel.2025.138232
38. Yin Z. Z., Ma J. M., Zhao B., et al. (2026). PVA-based hydrogen-bonded supramolecular adhesive with core-shell nanoarchitectures for multifunctional and sustainable applications. *J. Adv. Res.* **85**:615–631. DOI:10.1016/j.jare.2025.10.051
39. Ban L., Zhang Y., Sun D., et al. (2025). Photocatalytic hydrogen evolution driven by advanced metal sulfides from sustainable multilevel biomass and waste plastics. *Adv. Funct. Mater.* **35**:2506114. DOI:10.1002/adfm.202506114
40. Afewerki S. and Edlund U. (2023). Combined catalysis: A powerful strategy for engineering multifunctional sustainable lignin-based materials. *ACS Nano* **17**:7093–7108. DOI:10.1021/acsnano.3c00436
41. Osterberg M., Henn K. A., Farooq M., et al. (2023). Biobased nanomaterials-the role of interfacial interactions for advanced materials. *Chem. Rev.* **123**:2200–2241. DOI:10.1021/acs.chemrev.2c00492
42. Kirui A., Zhao W., Deligey F., et al. (2022). Carbohydrate-aromatic interface and molecular architecture of lignocellulose. *Nat. Commun.* **13**:538. DOI:10.1038/s41467-022-28165-3
43. Rahimi A., Ulbrich A., Coon J. J., et al. (2014). Formic-acid-induced depolymerization of oxidized lignin to aromatics. *Nature* **515**:249–252. DOI:10.1038/nature13867
44. Li Q., Dong Y., Hammond K. D., et al. (2021). Revealing the role of hydrogen bonding interactions and supramolecular complexes in lignin dissolution by deep eutectic solvents. *J. Mol. Liq.* **344**:117779. DOI:10.1016/j.molliq.2021.117779
45. Zhang Y., Zhou Y., Patria R. D., et al. (2025). Formic acid drives lignin valorization: Multiple pathways to value-added products. *Innov. Mater.* **3**:100139. DOI:10.59717/j.xinn-mater.2025.100139
46. Singh S. K. (2022). Ionic liquids and lignin interaction: An overview. *Bioresour. Technol. Rep.* **17**:100958. DOI:10.1016/j.biteb.2022.100958
47. Kang X., Kirui A., Dickwella Widanage M. C., et al. (2019). Lignin-polysaccharide interactions in plant secondary cell walls revealed by solid-state NMR. *Nat. Commun.* **10**:347. DOI:10.1038/s41467-018-08252-0
48. Talebi Amiri M., Bertella S., Questell-Santiago Y. M., et al. (2019). Establishing lignin structure-upgradeability relationships using quantitative 1H–13C heteronuclear single quantum coherence nuclear magnetic resonance (HSQC-NMR) spectroscopy. *Chem. Sci.* **10**:8135–8142. DOI:10.1039/c9sc02088h
49. Aida T., Meijer E. and Stupp S. (2012). Functional supramolecular polymers. *Science* **335**:813–817. DOI:10.1126/science.1205962
50. Lundberg D. J., Brown C. M., Bobylev E. O., et al. (2024). Nested non-covalent interactions expand the functions of supramolecular polymer networks. *Nat. Commun.* **15**:3951. DOI:10.1038/s41467-024-47666-x
51. Fu R., Xiao C., Du Z., et al. (2026). Switchable supramolecular adhesive by tuning interfacial bonding and modulus. *Adv. Funct. Mater.* **36**:e23966. DOI:10.1002/adfm.202523966
52. Xie X., Li R., Qiao Y., et al. (2025). An in-situ assembled cobweb-like adhesive with high processability. *Nat. Commun.* **16**:4872. DOI:10.1038/s41467-025-60076-x
53. Seiffert S. and Sprakel J. (2012). Physical chemistry of supramolecular polymer networks. *Chem. Soc. Rev.* **41**:909–930. DOI:10.1039/c1cs15191f
54. Zhang S., Koskela S., Meinhard H., et al. (2025). Multiscale interface engineering enables strong and water resistant wood bonding. *Nat. Commun.* **16**:7902. DOI:10.1038/s41467-025-63239-y
55. Han P. C., Chuang C. H., Lin S. W., et al. (2024). Phase-transformable metal-organic polyhedra for membrane processing and switchable gas separation. *Nat. Commun.* **15**:9523. DOI:10.1038/s41467-024-53560-3
56. Chen G., Fu S., Liu R., et al. (2010). Analysis of structural changes of masson pine lignin reacted with superoxide anion radical using nmr spectroscopy. *BioResources* **5**:1156–1163. DOI:10.15376/biores.5.2.1156-1163
57. Meng X., Crestini C., Ben H., et al. (2019). Determination of hydroxyl groups in biorefinery resources via quantitative ^{31}P NMR spectroscopy. *Nat. Protoc.* **14**:2627–2647. DOI:10.1038/s41596-019-0191-1
58. Bujosa S., Doncel-Gimenez A., Baumer N., et al. (2022). Thermoreversible polymorph transitions in supramolecular polymers of hydrogen-bonded squaramides. *Angew. Chem. Int. Ed.* **61**:e202213345. DOI:10.1002/anie.202213345
59. Rahimidehgolan F. and Altenhof W. (2023). Compressive behavior and deformation mechanisms of rigid polymeric foams: A review. *Compos. Pt. B-Eng.* **253**:110513. DOI:10.1016/j.compositesb.2023.110513
60. Xu J., Chen K., Maturilli A., et al. (2025). Biomass-derived polysilsesquioxane nanofilament reinforced porous aerogel for durable passive radiative cooling across all day and weather conditions. *ACS Nano* **19**:38395–38407. DOI:10.1021/acsnano.5c11008
61. General Administration of Quality Supervision, Inspection and Quarantine of the People's Republic of China, and Standardization Administration of China (2012). Classification for burning behavior of building materials and products (GB 8624-2012). Beijing, China.
62. Yang H., Yu B., Xu X., et al. (2020). Lignin-derived bio-based flame retardants toward high-performance sustainable polymeric materials. *Green Chem.* **22**:2129–2161. DOI:10.1039/d0gc00449a
63. Liu H. and Zhao X. (2022). Thermal conductivity analysis of high porosity structures with open and closed pores. *Int. J. Heat Mass Transf.* **183**:122089. DOI:10.1016/j.ijheatmasstransfer.2021.122089
64. Kumar D., Alam M., Zou P. X. W., et al. (2020). Comparative analysis of building insulation material properties and performance. *Renew. Sust. Energ. Rev.* **131**:110038. DOI:10.1016/j.rser.2020.110038
65. Barker-Rothschild D., Chen J., Wan Z., et al. (2025). Lignin-based porous carbon adsorbents for CO2 capture. *Chem. Soc. Rev.* **54**:623–652. DOI:10.1039/d4cs00923a

FUNDING AND ACKNOWLEDGMENTS

This work was supported by the National Natural Science Foundation of China (32271972) and 5·5 Engineering Research & Innovation Team Project of Beijing Forestry University (No. BLRC 2023B05). The funders had no role in study design, data collection and analysis, decision to publish, or preparation of the manuscript.

AUTHOR CONTRIBUTIONS

Xin-Yi Hui: Methodology, Formal analysis, Visualization, Writing—review & editing, Investigation, Writing—original draft. **Cheng Zuo:** Formal analysis, Visualization, Writing—review & editing. **Ji-Yun Qi:** Visualization, Formal analysis. **Chu-Wan Liang:** Visualization. **Tong Zhou:** Formal analysis. **Xiaojun Shen:** Writing—review & editing. **Jia-Long Wen:** Conceptualization, Methodology, Resources, Data curation, Visualization, Writing—review & editing, Supervision, Validation. **Tong-Qi Yuan:** Validation, Data curation, Supervision, Resources.

DECLARATION OF INTERESTS

The authors declare that they have no known competing financial interests or personal relationships that could have appeared to influence the work reported in this paper.

DATA AND CODE AVAILABILITY

All data supporting the findings of this study are available within the article and its supplemental information. Additional information is available from the corresponding author upon reasonable request. This study did not generate original code.

SUPPLEMENTAL INFORMATION

It can be found online at https://doi.org/10.59717/j.xinn-mater.2026.100243.